Volume 6 | Number 9 | September 2014 | Pages 1567–1760

Metallomics

www.rsc.org/metallomics

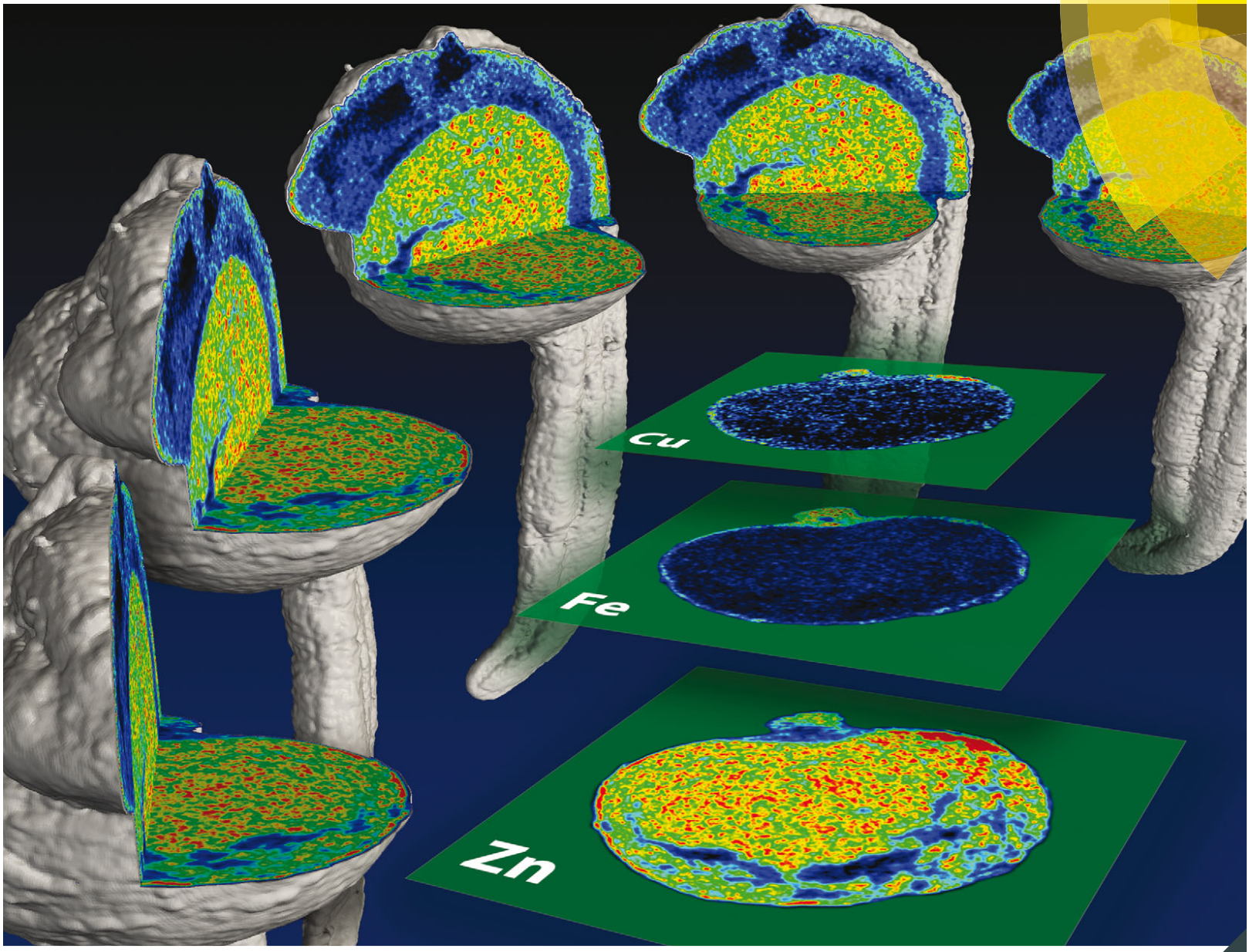

ISSN 1756-5901

ROYAL SOCIETY OF CHEMISTRY

PAPER
Christoph J. Fahrni *et al.*
3D imaging of transition metals in the zebrafish embryo by X-ray fluorescence microtomography

Indexed in Medline!

Metallomics

PAPER

View Article Online
View Journal | View Issue

Cite this: *Metallomics*, 2014, 6, 1648

3D imaging of transition metals in the zebrafish embryo by X-ray fluorescence microtomography†

Daisy Bourassa,[a] Sophie-Charlotte Gleber,[b] Stefan Vogt,[b] Hong Yi,[c] Fabian Will,[d] Heiko Richter,[d] Chong Hyun Shin[e] and Christoph J. Fahrni*[a]

Received 28th April 2014,
Accepted 20th June 2014

DOI: 10.1039/c4mt00121d

www.rsc.org/metallomics

Synchrotron X-ray fluorescence (SXRF) microtomography has emerged as a powerful technique for the 3D visualization of the elemental distribution in biological samples. The mechanical stability, both of the instrument and the specimen, is paramount when acquiring tomographic projection series. By combining the progressive lowering of temperature method (PLT) with femtosecond laser sectioning, we were able to embed, excise, and preserve a zebrafish embryo at 24 hours post fertilization in an X-ray compatible, transparent resin for tomographic elemental imaging. Based on a data set comprised of 60 projections, acquired with a step size of 2 μm during 100 hours of beam time, we reconstructed the 3D distribution of zinc, iron, and copper using the iterative maximum likelihood expectation maximization (MLEM) reconstruction algorithm. The volumetric elemental maps, which entail over 124 million individual voxels for each transition metal, revealed distinct elemental distributions that could be correlated with characteristic anatomical features at this stage of embryonic development.

Introduction

Transition metals such as zinc, copper, and iron are essential trace nutrients for all forms of life. As cofactors in metalloproteins, they play pivotal roles in a broad range of biological processes, including respiration, metabolic pathways, and gene regulation.[1] To ensure a sufficient supply, nature has evolved an intricate network of proteins that acquire, distribute, and regulate these metals. Not surprisingly, the disruption of this regulatory machinery may lead to metal overload or deficiency, which are the hallmarks of diseases such as Parkinson's disease,[2] Alzheimer's disease,[3] Menkes' disease, and Wilson's disease.[4] To understand the mechanisms that govern transition metal homeostasis, a detailed knowledge of the metal ion distribution inside cells, tissues, and whole organisms is essential.

Several modern microanalytical techniques, including secondary ion mass spectrometry (SIMS), electron-probe X-ray microanalysis (EPXMA), nuclear microprobes (proton-induced X-ray emission), and synchrotron X-ray fluorescence (SXRF) microscopy, are capable of quantifying trace metals within cells and tissue sections to yield 2D maps at submicron spatial resolution.[5] As SXRF microscopy operates in the hard X-ray energy regime, this technique can be employed to visualize the elemental content of thick hydrated tissues or small organisms such as nematodes[6] and zebrafish embryos;[7] however, the resulting 2D maps correspond to projections of the integrated metal content along the excitation trajectory and thus fail to provide unambiguous insights into the actual 3D structural organization. Given the advances in X-ray imaging technology, notably the development of multi-element detectors with improved sensitivity, as well as detector electronics with fast readout, data acquisition times have been significantly shortened, thus enabling the visualization of the 3D elemental distributions based on tomographic projection series.[8] For example, SXRF microtomography has been employed to study the iron distribution in wild-type and mutant *Arabidopsis* seeds lacking an iron uptake transporter,[9] and more recently, de Jonge *et al.* succeeded in visualizing the quantitative 3D elemental distribution in a diatom[10] and in *C. elegans*.[11]

In all cases, the elemental distribution was reconstructed from 2D SXRF projection maps, which were acquired by scanning the specimen through the stationary beam at varying projection angles. This approach requires that the sample has sufficient mechanical stability for mounting on a rotational stage, a limiting prerequisite when attempting to image soft specimens such as zebrafish embryos or thick tissue sections. To address

[a] *School of Chemistry and Biochemistry and Petit Institute for Bioengineering and Bioscience, Georgia Institute of Technology, 901 Atlantic Drive, Atlanta, GA 30332, USA. E-mail: fahrni@chemistry.gatech.edu*
[b] *Advanced Photon Source, X-ray Science Division, Argonne National Laboratory, 9700 S. Cass Avenue, Argonne, IL 60439, USA*
[c] *Robert P. Apkarian Integrated Electron Microscopy Core, Emory University, 1521 Dickey Drive, Atlanta, GA 30322, USA*
[d] *LLS Rowiak LaserLabSolutions GmbH, Garbsener Landstrasse 10, D-30419 Hannover, Germany*
[e] *School of Biology and Petit Institute for Bioengineering and Bioscience, Georgia Institute of Technology, 310 Ferst Drive, Atlanta, GA 30332, USA*

† Electronic supplementary information (ESI) available: Figures and video animations as mentioned in the text. See DOI: 10.1039/c4mt00121d

this challenge, we employed an embedding method commonly used in electron microscopy preparations and excised the specimen by femtosecond laser sectioning from the polymer block for tomographic imaging. Using a zebrafish embryo as a test sample, we were able to preserve its structural integrity, acquire a complete set of tomographic projections, and reconstruct the 3D distribution of zinc (Zn), copper (Cu), and iron (Fe) at a spatial resolution around 5 μm.

Experimental

Sample preparation

Adult wild-type zebrafish were housed and mated under standard laboratory conditions. Fertilized embryos were harvested and kept in E3 medium (5 mM NaCl, 0.17 mM KCl, 0.4 mM $CaCl_2$ and 0.16 mM $MgSO_4$) at 28.5 °C. At 24 hours post fertilization (hpf), embryos were anesthetized in 0.2% Tricane, dechorionated, and fixed with 4% paraformaldehyde in 0.1 M sodium phosphate buffer (pH 7.4) at 4 °C. After two hours in the fixative, embryos were washed three times with the same buffer, dehydrated in ethanol, and then embedded in Lowicryl K4M resin at −20 °C following the progressive lowering of temperature (PLT) protocol.[12] The polymer block containing the zebrafish embryo was trimmed with a diamond saw (Buehler Isomet 1000, Germany) coplanar to the frontal plane on the ventral side of the embryo. The resulting plane was mounted onto a microscope slide with UV curing glue (Panacol Vitralit, Germany), and 4 contact-free line sections around the embryo were performed with a femtosecond laser system (TissueSurgeon, LLS Rowiak LaserLabSolutions, Germany). Two of the sections were placed on each lateral side at a distance of 60 μm from the embryo, one section at 60 μm from the caudal end and perpendicular to the two lateral sections, and one section at 500 μm from the cranial end of the embryo, again perpendicular to the lateral sections. To remove metal contaminations and ridges from the diamond saw, an additional coplanar section below the ventral side of the embryo was performed at a distance of 60 μm from the embryo. For sample adjustment and quality control, optical coherence tomography (OCT) images were acquired with a spectral radar system (Thorlabs) modified for integration in TissueSurgeon. The peak wavelength of the OCT light source is 930 nm, offering an axial resolution of 5–7 μm and lateral resolution of <5 μm within the focal plane. Brightfield images were acquired with an integrated CCD-camera (768 × 494 pixel size). Illumination was realized with a custom-made condenser and a high power LED at a wavelength of 800 nm for optimal transmission across the NIR-optimized objective lens. The excised sample was attached with epoxy glue along the cranial surface onto an aluminum holder for mounting on the kinematic stage of the SXRF tomography setup.

Instrumentation

Synchrotron radiation X-ray fluorescence (SXRF) tomography data were acquired at the 2-ID-E beamline of the Advanced Photon Source (Argonne National Laboratory, Illinois, USA). The beamline is equipped with an undulator and double monochromator, which provide high brilliance X-rays with a tunable energy range between 8–20 keV. The X-ray beam is focused to a spot size of 0.6 × 0.5 μm^2 using the first order diffraction peak of a 320 μm diameter Fresnel zone plate (Xradia, Carl Zeiss, Germany). Higher order diffraction peaks and scattered photons are blocked by a 30 μm diameter tungsten pinhole (order sorting aperture), which is positioned 10 mm upstream of the sample. To minimize scatter signals from air and ambient argon fluorescence, the sample is placed inside a helium-filled chamber equipped with a kapton window for beam entrance. The sample is mounted on an aluminum stick and placed onto a kinematic holder controlled by a stack of 3 piezo-encoded stages (Physik Instrumente GmbH, Germany), a rotation stage and two lateral stages for aligning the sample along the tomographic rotation axis. For raster-scanning of the sample, the entire chamber is moved by two additional vertical and horizontal stages, which offer step sizes down to 50 nm, and if desired, travel distances up to several millimeters. For each focused spot, a full fluorescence spectrum is acquired using an energy dispersive silicone drift detector (Vortex ME-4 by SII Nano Technology, Northridge, CA) positioned at 90 degrees to the incident beam. The detector snout is placed inside the sample chamber and covered with an off-center aluminum collimator specifically designed for the geometry of the 4-element fluorescence detector. A second kapton window allows the beam to reach a downstream ion chamber for monitoring the signal intensity after passing the sample and all optical components. The change in signal intensity compared to the upstream ion chamber provides an absorption contrast signal of the sample. At the downstream end of the microprobe the transmitted beam enters a custom-built configured charge-integrating silicon detector, which provides differential phase contrast.[13] All motorized stages are controlled through EPICS (Experimental Physics and Industrial Control System, Argonne National Laboratory).

Data acquisition

The SXRF tomographic data set of the zebrafish specimen was composed of 60 projections acquired at intervals of 3 degrees covering a total angular space of 180 degrees. To minimize errors introduced through radiation damage and potential registration drifts, the projections were acquired in two batches with a 3 degree offset and 6 degree intervals. For each orientation, the specimen was translated through the stationary beam with excitation at 10 keV and a step size of 2 μm, covering a total scan area of 840 × 1562 μm. To minimize the data collection time, horizontal scans were acquired in a continuous motion mode[14] with an average dwell time of 10 ms per pixel. Composed of ∼20 million individual emission spectra, the complete tomographic data set required over 100 hours of beam time.

Data processing and tomographic reconstruction

For each projection angle elemental maps were generated by Gaussian fitting of the averaged raw emission spectra from 3 × 3 adjacent pixels (2D boxcar averaging) using the MAPS software package.[15] The Gaussian peaks were matched to the characteristic X-ray emission lines to determine the fluorescence

signal for Zn, Cu, and Fe. Calibration to elemental densities ρ (μg cm^{-2}) was achieved by comparing the fluorescence emission of the sample with that of a thin film standard (Axo Dresden, Germany) relative to the photon flux captured by two ion chambers positioned upstream and downstream of the sample (see also above description of the instrumentation). Due to signal attenuation by the resin, calibration relative to the up- and downstream photon fluxes yielded either underestimated or overestimated densities ρ_{us} and ρ_{ds}, respectively. The two values are related to the linear attenuation coefficient μ_{ex} and attenuation pathlength l according to the Beer–Lambert law (1)

$$\rho_{us} = \rho_{ds} \cdot e^{-l\mu_{ex}} \quad (1)$$

The absorption contrast generated by the sample can be judged based on the ratio between the photon counts of the upstream and downstream ion chambers. Concluding from the transmission profile across the sample, the embedding material is responsible for the majority of the beam attenuation (Fig. S1, ESI†). With excitation at 10 keV, the transmission is reduced to 77% across the pathlength of the Lowicryl matrix, and only lowered to 75% by the yolk, which corresponds to the largest volume of the specimen. For this reason, we approximated the elemental concentrations in the reconstructed model only based on the corresponding linear attenuation coefficients of the matrix and the average attenuation pathlength l (see ESI,† for details). The 3D elemental distributions were reconstructed based on downstream-calibrated projections, which were imported into MATLAB (R2012b),[16] normalized to the integrated density averaged over all projections, and processed using custom made MATLAB codes. For reconstructions based on the filtered back projection algorithm, the elemental maps were processed with the *iradon* routine using the ''Ram–Lak'' ramp-filter as implemented in the MATLAB Image Processing Toolbox. The code for maximum likelihood expectation maximization (MLEM) reconstruction was derived from the standard iterative algorithm[17] employing the *radon* and unfiltered *iradon* MATLAB routines for projection and back-projection, respectively. Prior to processing of the actual experimental data set, the performance of the code was evaluated based on the reconstruction accuracy of a computer generated Shepp–Logan phantom image (ESI,† Fig. S2). To generate volumetric elemental distributions, sinograms were derived for each of the 781 *y*-positions and the corresponding 2D elemental densities were iteratively reconstructed using the MLEM code. For the reconstruction of the Zn distribution a total of 70 iterations were employed. To improve signal-to-noise ratios, the Fe and Cu data sets were processed with smaller iteration numbers of 30 and 15, respectively. To gauge the quality of the reconstructed volumetric data sets, projections for each of the 60 acquisition angles were computed and the corresponding difference images derived based on the original measured projections (ESI,† Fig. S3). The final elemental distributions were estimated by converting the pixel-based area densities of each slice to voxel-based concentrations, followed by linear scaling as described in the ESI.†

Data visualization

All volumetric renderings were generated with the Paraview software package.[18] For this purpose, the reconstructed volumetric data were exported from MATLAB as 32-bit *z*-stacks, converted to 16-bit stacks using ImageJ,[19] and then imported into Paraview for 3D processing and visualization.

Results

Specimen preparation and femtosecond laser sectioning

Initial attempts to use high-pressure freezing for preserving the zebrafish embryos at 24 hours post fertilization (hpf) led to fractures, likely due to insufficient cooling rates associated with specimens of this size. Therefore, the embryos were fixed first in paraformaldehyde solution and then embedded by the progressive lowering of temperature (PLT) method.[12]

Due to attenuation of the X-ray fluorescence signal by the polymer matrix, it is advantageous to trim the resin block as close as possible to the specimen. Although traditional microtomes are designed to cut thin sections with high precision, they are ill-suited to excise a three-dimensional structure from a block. To address this challenge, we explored the utility of a commercial femtosecond laser-based microtome system (TissueSurgeon, LLS Rowiak LaserLabSolutions, Germany). As illustrated with Fig. 1, we were able to excise the embedded embryo by 4 lateral contact-free line sections (A) followed by a coplanar section on the ventral side that released the cube from the resin block (B). Based on this approach we successfully removed the extraneous resin at a distance of 60 μm from the embryo while preserving the integrity of the embryo as shown by the near-infrared brightfield micrograph (C).

Data acquisition and tomographic reconstruction

Synchrotron radiation X-ray fluorescence (SXRF) tomography data were acquired at the 2-ID-E beamline of the Advanced Photon Source. A schematic representation of the instrument is shown in Fig. 1D, and a description of the individual components is provided in the experimental section. For tomographic reconstruction of the 3D elemental distributions, we acquired a total of 60 projections spread over an angular space of 180 degrees. The data were collected in two batches with a 3 degree offset and 6 degree intervals. Despite the long acquisition time of over 100 hours, radiation damage appeared negligible as judged from the differences in integrated photon counts between the two batches.

As the X-ray fluorescence tomography setup shown in Fig. 1D yields parallel beam projections, the tomography data could be in principle processed with the same algorithms developed for absorption-based X-ray computed tomography (X-ray CT). The most common approach for the three-dimensional reconstruction of CT data is based on the filtered back projection algorithm (FBP), in which an inverse radon transform is combined with a ramp-filter to address image blurring.[17] As illustrated with Fig. 2A, this algorithm is however not well suited for the reconstruction of fluorescence-based data sets, which are

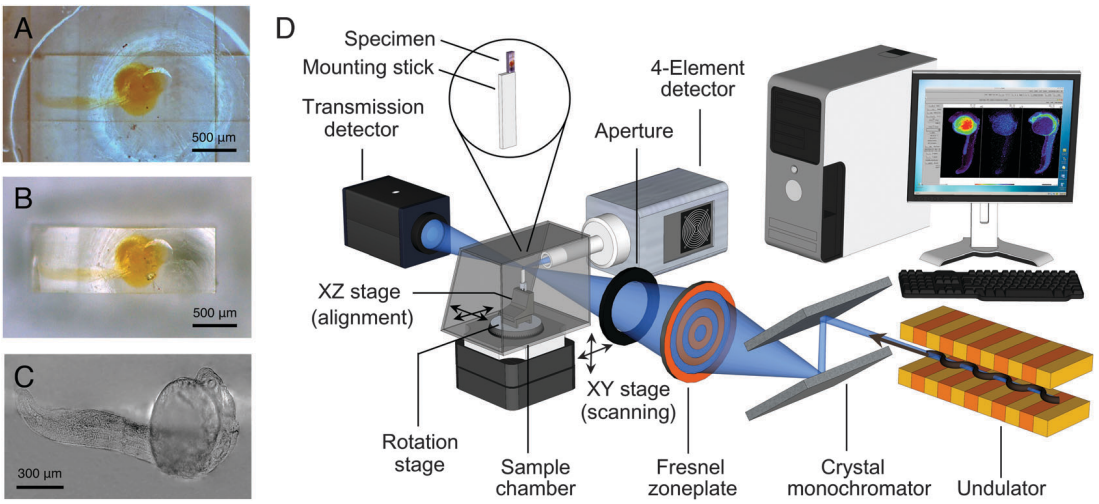

Fig. 1 X-ray tomography of zebrafish embryos. (A–C) Preparation of resin embedded specimens for X-ray fluorescence tomography using a femtosecond laser sectioning microtome system (TissueSurgeon, LLS Rowiak LaserLabSolutions, Germany). A zebrafish embryo at 24 hpf was fixed and embedded in resin (Lowicryl K4M) by the progressive lowering of temperature method (PLT). The cured resin block was mounted on a microscope slide and trimmed by 4 contact-free lateral line sections (A) followed by a coplanar section on the ventral side of the embryo (B). The near-infrared (800 nm) brightfield image (C) confirmed the integrity of the specimen. (D) Schematic illustration of the X-ray fluorescence tomography instrument at the 2-ID-E beam line at the Advanced Photon Source (Argonne National Laboratory, USA). The excised specimen (B) was attached to an aluminum stick (circle inset), mounted on the *xz*/rotation stage, and raster-scanned through the focused beam for each projection angle. The emitted photons were captured by an energy-dispersive X-ray detector and the raw data were processed with the MAPS[15] and MATLAB software packages (see text for details).

comprised of fewer projections and characterized by a lower signal-to-noise ratio compared to conventional X-ray CT. In the case of the Cu data set, the overpowering noise made it difficult to discern any contours in the reconstructed image (Fig. 2A, 3rd row). In addition, the FBP algorithm produced substantial streak artifacts in the reconstructed images of all three elements due to the limited number of projections covering the 180° angular space.

To reduce the noise level and streak artifacts in the reconstructed model, we explored the utility of the iterative maximum likelihood expectation maximization (MLEM) algorithm. Originally developed for the reconstruction of positron emission tomography

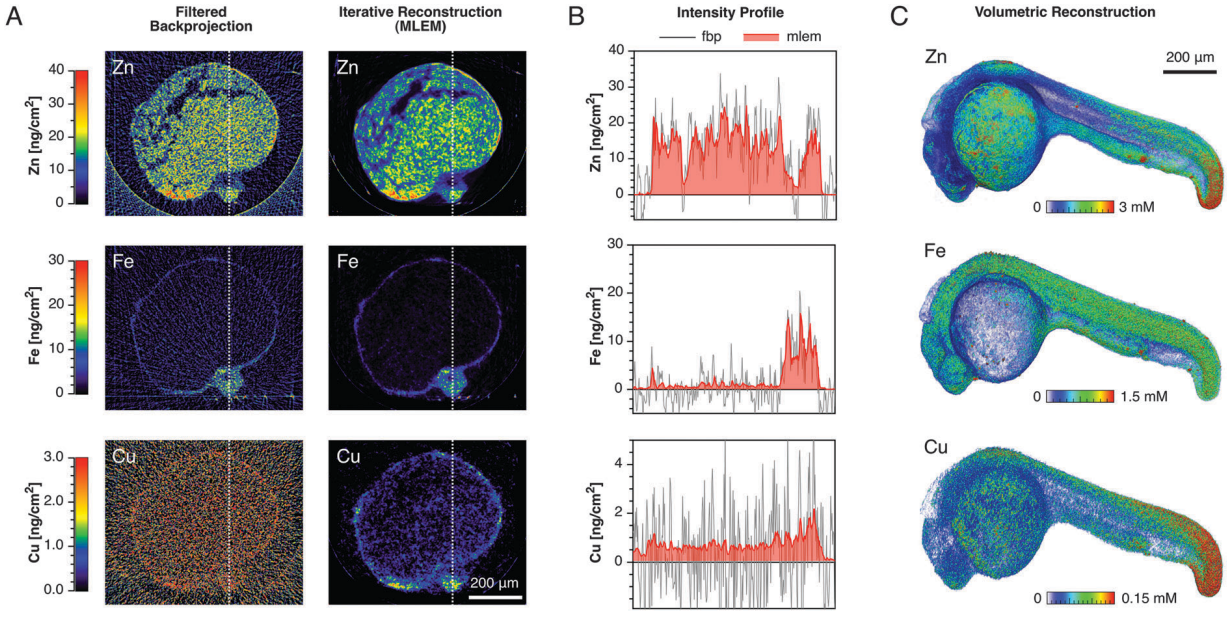

Fig. 2 Tomographic reconstruction of the elemental densities of Zn, Fe, and Cu based on the corresponding SXRF emission projection data sets. (A) Comparison of the reprojected elemental densities based on a filtered back projection algorithm with Ramachandran–Lakshminarayanan (“Ram–Lak”) ramp-filter and an iterative maximum likelihood expectation maximization (MLEM) algorithm. The MLEM algorithm leads to significantly improved reconstructions in the case of noisy datasets. (B) Intensity profile of the reconstructed density images shown in (A) along the white dashed line. The fluorescence detector was positioned on the left side relative to the reconstructed images of panel (A). (C) Complete volumetric reconstruction for each element (rendered with Paraview;[18] ESI,† Video S1).

(PET) data,[17,20] this algorithm utilizes a noise model based on the Poisson distribution of the photons arriving at the detector. In addition to being less sensitive towards projection noise compared to FBP, the MLEM algorithm has the advantage to yield back projections with only positive densities as illustrated with the profiles in Fig. 2B. Furthermore, the noise level is reduced at lower iteration numbers, though at the expense of image resolution (ESI,† Fig. S2). Based on this approach, we were able to reconstruct the Zn, Fe and Cu distributions with significant detail using the iteration numbers of 70, 30 and 15, respectively.

To account for attenuation of the excitation and fluorescence emission by the polymer matrix, we derived linear scaling factors based on the average pathlength and the corresponding energy dependent attenuation coefficients (see ESI†). Because the tomographic projections cover only half of the 360 degree angular space, the resulting back projections are expected to falloff along the excitation axis. To evaluate the error associated with simple linear scaling, we performed a series of simulations using the *raft* library, a collections of subroutines developed for X-ray fluorescence tomography computations.[21] A phantom image was placed within a uniform attenuation matrix that matched the average experimental pathlength of 680 μm (Fig. S4, ESI†). We then computed sinograms with and without consideration of the excitation and emission attenuation (Fig. S4A, ESI†), performed reconstructions using the filtered back projection or MLEM algorithms, and corrected the resulting images by applying the corresponding linear scaling factors (Fig. S4B and C, ESI†). In the case of Zn, the attenuation coefficient for the Kα emission in Lowicryl is small relative to the pathlength ($\mu_{K\alpha Zn}$ = 5.16 cm^{-1}), and resulted in little deviations from the original image. Only at the periphery of the phantom the error exceeded 5% (Fig. S4C, ESI†). By comparison, the attenuation coefficient for Fe is higher ($\mu_{K\alpha Fe}$ = 12.71 cm^{-1}), and thus resulted in a more pronounced intensity falloff with a maximum error of 20% in the peripheral region (Fig. S4D, ESI†). Altogether, we concluded that the simple linear scaling approach should yield good approximations for the actual Zn distribution, and quite reasonable estimates for Fe with this size of sample. Based on the scaled MLEM data, we determined a total Zn content of 6.7 ng, which is in good agreement with the average Zn content of ~7.3 ng at 24 hpf reported in the literature.[22]

To generate the final 3D models, we utilized the MLEM algorithm to reconstruct 2D slices from each of the 781 line sinograms and applied the corresponding linear scaling factors. This procedure resulted in sets of volumetric data, each composed of over 124 million 2 × 2 × 2 × μm^3 voxels. As evident from the corresponding 3D renderings in Fig. 2C (ESI,† Video S1), the transition metals show distinct distributions that can be correlated with characteristic anatomical features of the developing zebrafish.[23]

3D elemental distributions

At 24 hpf, the embryo has just transitioned out of segmentation into the pharyngula period, which is characterized by a well-developed notochord, an elongated tail, and a brain that has been sculpted into distinguishable lobes and ventricles.[24] To illustrate the most pertinent aspects of the Zn, Fe, and Cu distributions, Fig. 3 shows a series of virtual sagittal, coronal, and transverse sections of the embryo. The position of each slice is depicted in column A in the form of a 3D rendering, and the corresponding 2D elemental maps are arranged in column B. To accommodate the differences in dynamic range between the elements, the false-color maps are reproduced with different concentration scales. Furthermore, column C features normalized dual-color overlays to visualize the relative spatial relationships between pairs of elements. A complete set of the coronal, sagittal, and transverse sections with 2 μm spacing is provided in the ESI† as video animations (ESI,† Video S2A–C).

Among the three metals, Zn is the most abundant with concentrations approaching up to 7 mM (Fig. 3B). The most significant pool, comprising more than 80% of the total Zn content, is found in the yolk (yo) and yolk extension (ye) (Fig. 3, 1st and 2nd row). The early pharyngula period is also marked by the formation of the circulatory system, and the presence blood vessels (bv) can be already recognized as voids within the Zn distribution of the yolk. These blood vessels, such as the common cardinal veins or ducts of Cuvier, carry blood ventrally across the yolk to supply blood to the heart.[25] The Zn distribution can be further correlated with structures of the nervous system such as the notochord (nc), the neural tube (nt), and the brain. Similar to the blood vessels, the notochord region is marked by a low metal content, whereas the neural tube is set apart by areas of high Zn (Fig. 3B, 1st row, transverse section). The ventricles of the brain appear as voids within the Zn maps; specifically, the third (tv) and fourth (fv) ventricles can be identified in the sagittal section (Fig. 3B, 1st row). While the ventricles uniformly exhibit low trace metal levels, various regions of the grey matter can be identified, including the mesencephalon (mc), cerebellum (cb), the telencephalon (tc) and diencephalon (dc) of the forebrain, and the rhombencephalon (rc) of the hindbrain. Finally, the sagittal section (Fig. 3, 3rd row) reveals a distinct accumulation of Zn at the tip of the tail (tl), mostly localized to peripheral cell layers. Altogether, this area exhibits the highest concentration of Zn within the embryo.

By comparison, the Fe distribution appears less localized with maximum concentrations not exceeding 2 mM. As evident from the overlays in Fig. 3C (1st column), Fe and Zn are distributed in an anti-correlated fashion throughout most regions of the embryo. A detailed analysis revealed two distinct populations of voxels with anti-correlated Zn and Fe contents as well as a low Pearson's correlation coefficient of 0.117 (ESI,† Fig. S5). The highest concentration of Fe can be found in the medial region of the tail as well as in areas of the brain, whereas the yolk and yolk extension are characterized by overall low Fe levels. Instead, both structures are surrounded by a thin Fe veneer, which does not overlap with regions of high Zn. Similarly, the areas of high Zn at the tip of the tail are low in Fe and set apart from the Fe-rich regions in the medial body. Although Zn and Fe are anti-correlated throughout most of the embryo, there are still a few notable similarities. For example, the notochord appears to

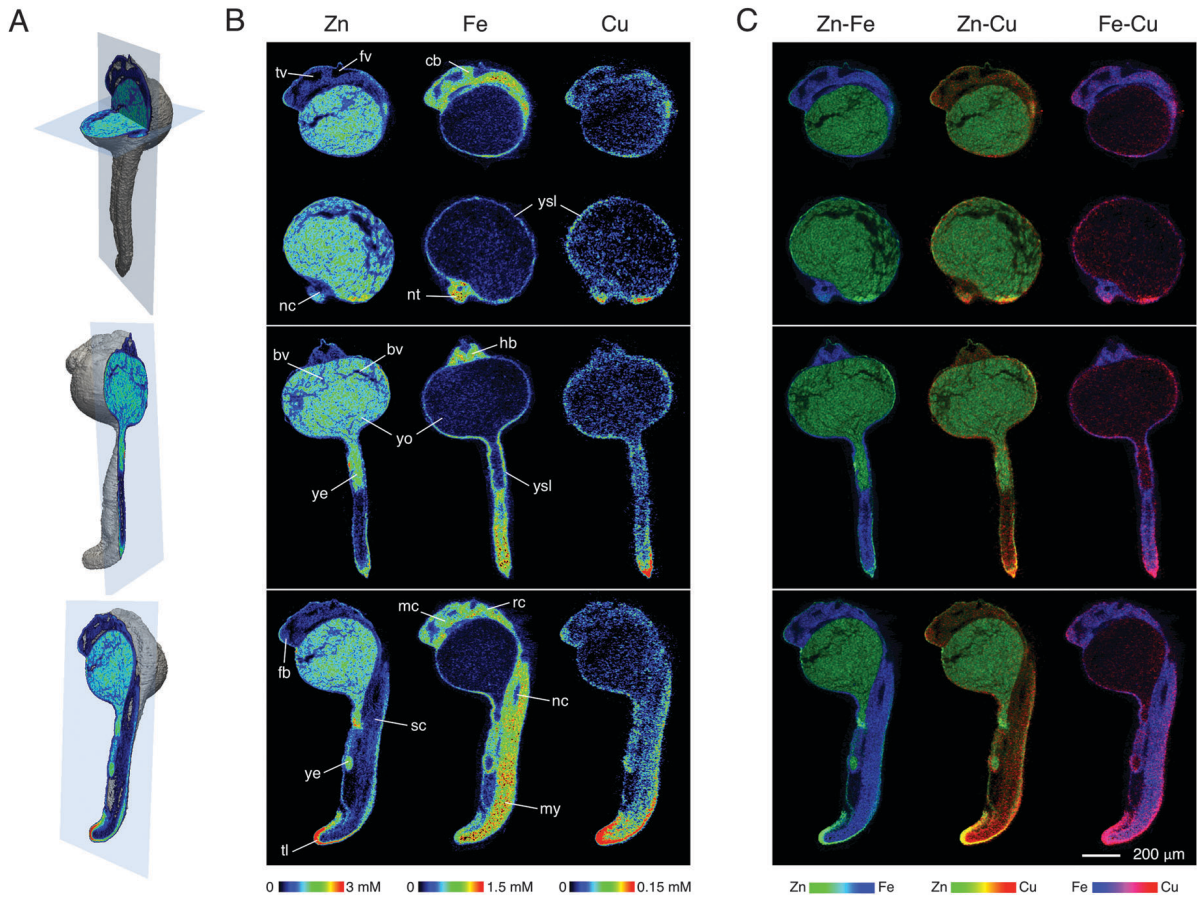

Fig. 3 Visualization of the elemental distribution in a zebrafish embryo (24 hpf) by X-ray fluorescence tomography (MLEM reconstruction). (A) 3D-rendering of the embryo indicating the spatial orientation of the virtual slices that are displayed in panels (B) and (C). Slices include a sagittal and transverse section (top), a coronal section (middle), and a sagittal section offset to the left (bottom). (B) Elemental distributions of Zn, Fe, and Cu for each of the 4 slices. Individual concentration scales for each element are displayed at the bottom of each column. Abbreviations: third ventricle (tv), fourth ventricle (fv), cerebellum (cb), notochord (nc), neural tube (nt), blood vessels (bv), hindbrain (hb), yolk (yo), yolk extension (ye), yolk syncytial layer (ysl), myotome (my), telencephalon (tc), mesencephalon (mc), diencephalon (dc), rhombencephalon (rc), and tail (tl). (C) False-color overlays of the elemental distributions of Zn, Fe, and Cu indicating regions of colocalization. The concentration scales of each element were normalized and color-coded as follows: Zn (green), Fe (blue), and Cu (red). Areas of colocalization appear in the corresponding mixed hues.

be void of Fe, whereas the neighboring neural tube contains a much higher concentrations of Fe. Similar to Zn, the anatomical features of the brain can be readily recognized based on the Fe distribution.

Given the low concentration of Cu throughout the embryo, the reconstructed data set is of lower quality and characterized by a significant level of background noise. Nevertheless, the 3D model revealed distinct regions that could be correlated with the Zn and Fe distributions. Most notable is the high concentration of Cu located at the tip of the tail also observed for Zn. The high degree of colocalization between the two metals is apparent in the overlay plot as orange-yellow regions (Fig. 3C, 3rd row). Similar to Fe, the Cu concentration within the yolk and yolk extension is low, but appears increased within a peripheral layer surrounding both structures.

Discussion

Compared to 2D SXRF imaging, the tomographic visualization of the 3D elemental distribution presents a host of additional challenges with regard to specimen preparation, instrument stability, and post-acquisition data processing. Previous tomographic SXRF studies focused on samples that either had sufficient mechanical stability for direct mounting on a rotational stage, or that could be placed on an X-ray compatible surface without damage. In the case of zebrafish embryos, neither of these methods would be successful. The approach described here, which combines an established embedding method with femtosecond laser sectioning, expands the type of specimens that can be investigated by X-ray fluorescence projection tomography.

The Lowicryl resin employed offers a number of advantages over other embedding media such as paraffin. It provides not only the necessary mechanical stability for tomographic mounting, but proved to be stable towards prolonged X-ray exposure without noticeable damage. As the resin is optically transparent in the visible to near-infrared wavelength range, it can be processed with a near-infrared femtosecond laser sectioning system, and the integrity of the sample can be confirmed by near-infrared brightfield imaging at any time during the excision procedure. Furthermore, Lowicryl has been shown to preserve the chromophores of fluorescent protein markers,[26] a property that could

be exploited for correlative imaging studies. For example, prior to conducting the tomographic elemental analysis, expressed fluorescent protein tags could be imaged within the embedded specimen by two-photon excitation microscopy.

Routinely used for the 3D visualization of PET data, the MLEM algorithm proved to be well suited for the back projection of X-ray fluorescence tomography data and yielded superior results over the traditional FBP algorithm. At present, the attenuation of the incident and emitted photons by the Lowicryl matrix has only been addressed by linear scaling factors, and therefore, the volumetric data do not correspond to precise elemental concentrations. Concluding from the attenuation simulations as well the absence of apparent intensity falloffs within the reconstructed *xz*-planes (Fig. 2A), however, we estimate that the derived concentrations are still accurate within an error margin of 20% or better. At the expense of spatial resolution or data acquisition time, a full 360 degree tomographic data set would yield more reliable reconstructed models, especially as the attenuation is dominated by the polymer matrix. The development of reconstruction methods that take into account matrix effects is an active area of research, and it will be critical to test these approaches against reference standards with known elemental compositions.[27]

The reconstructed elemental densities provided intriguing insights into the 3D distribution of Zn, Cu, and Fe at this stage of embryonic development. Most apparent are the large Zn stores in the yolk and yolk extension as well as the accumulation of Zn and Cu at the tip of the tail. The importance of Zn for cellular proliferation and growth is well established.[28] As the maternally derived yolk stores are the primary source of nutrients for the embryo, this pool supplies all developing tissues and organs with Zn, likely orchestrated through an elaborate network of Zn transporters.[22] For example, the reduced expression of Zip7, a Zn importer of the SLC39 solute carrier family of proteins, led to markedly decreased Zn levels in the eye at 72 hpf whereas the total Zn content of the embryo remained unaltered.[7] In contrast, both Fe and Cu are more concentrated in the yolk syncytial layer (YSL) surrounding the yolk and yolk extension. This extra-embryonic tissue serves critical functions in cell fate specification, morphogenesis, and nutrient transport.[29] The Fe transporters ferroportin1 and transferrin are specifically expressed in the YSL,[30] underscoring its role in Fe mobilization. Likewise, ceruloplasmin, the major Cu-carrying protein that also assists in Fe transport,[31] is localized to the YSL at this stage of development.[32] Furthermore, at 24 hpf, pigment formation is initiated by melanophores, which depend on Cu to supply the enzyme tyrosinase involved in melanogenesis.[33] The melanophores start to develop dorsolaterally throughout the body of the tail, an area that is also characterized by increased levels of Cu. Finally, the markedly increased levels of Zn and Cu at the posterior end of the embryo coincide with areas of progenitor cell differentiation[34] and cellular proliferation,[35] which are responsible for most of the body growth at this stage of development.[36] Recent X-ray fluorescence studies of *in vitro* mouse fibroblast cell cultures revealed 2- to 3-fold higher Zn levels in mitotic compared to interphase cells, underlining the prominent role of Zn during cellular proliferation.[37]

Conclusions

Our study demonstrates that X-ray fluorescence tomography has matured into a powerful technique for the high-resolution 3D visualization of transition metals, even for large specimens such as a zebrafish embryo. The volumetric elemental maps offered an intriguing view of the elemental distributions within the intact embryo, and revealed distinct areas of localizations that could be correlated with characteristic anatomical features at this developmental stage. The preparation technique, which combines the progressive lowering of temperature method with femtosecond laser sectioning, should be applicable to a wide range of soft tissue specimens. Extended to comparative studies of organisms with altered expression levels of specific proteins, this technique is well poised to illuminate the mechanisms of biological trace metal storage, transport, and regulation.

Conflicts of interest

FW and HR were funded through LLS Rowiak LaserLabSolutions GmbH, the manufacturer of the femtosecond laser microtome (TissueSurgeon) used in this work.

Acknowledgements

Financial support by the National Science Foundation (CHE-1306943 to CJF), the National Institutes of Health (K01DK081351 to CHS), and the Vasser Woolley Foundation is gratefully acknowledged. Use of the Advanced Photon Source was supported by the U.S. Department of Energy, Office of Science, Office of Basic Energy Sciences, under Contract No. DE-AC02-06CH11357.

Notes and references

1 I. Bertini, H. B. Gray, E. I. Stiefel and J. S. Valentine, *Biological Inorganic Chemistry: Structure and Reactivity*, University Science Books, 2007.
2 A. Takeda, *Brain Res. Rev.*, 2003, **41**, 79.
3 A. I. Bush, *Trends Neurosci.*, 2003, **26**, 207.
4 N. C. Andrews, *Curr. Opin. Chem. Biol.*, 2002, **6**, 181.
5 M. W. Bourassa and L. M. Miller, *Metallomics*, 2012, **4**, 721; C. J. Fahrni, *Curr. Opin. Chem. Biol.*, 2007, **11**, 121; E. Kosior, S. Bohic, H. Suhonen, R. Ortega, G. Deves, A. Carmona, F. Marchi, J. F. Guillet and P. Cloetens, *J. Struct. Biol.*, 2012, **177**, 239; R. McRae, P. Bagchi, S. Sumalekshmy and C. J. Fahrni, *Chem. Rev.*, 2009, **109**, 4780; R. Ortega, G. Deves and A. Carmona, *J. R. Soc., Interface*, 2009, **6**, S649; T. Paunesku, S. Vogt, J. Maser, B. Lai and G. Woloschak, *J. Cell. Biochem.*, 2006, **99**, 1489; Z. Qin, J. A. Caruso, B. Lai, A. Matusch and J. S. Becker, *Metallomics*, 2011, **3**, 28.
6 Y. Gao, N. Liu, C. Chen, Y. Luo, Y. Li, Z. Zhang, Y. Zhao, B. Zhao, A. Iida and Z. Chai, *J. Anal. At. Spectrom.*, 2008, **23**, 1121; S. A. James, M. D. de Jonge, D. L. Howard, A. I. Bush, D. Paterson and G. McColl, *Metallomics*, 2013, **5**, 627.

7 G. Yan, Y. C. Zhang, J. L. Yu, Y. Yu, F. Zhang, Z. Z. Zhang, A. M. Wu, X. H. Yan, Y. Zhou and F. D. Wang, *PLoS One*, 2012, **7**, e42939.
8 M. D. de Jonge and S. Vogt, *Curr. Opin. Struct. Biol.*, 2010, **20**, 606; P. Bleuet, P. Gergaud, L. Lemelle, R. Tucoulou, P. Cloetens, J. Susini, G. Delette and A. Simionovici, *TrAC, Trends Anal. Chem.*, 2010, **29**, 518.
9 S. A. Kim, T. Punshon, A. Lanzirotti, L. Li, J. M. Alonso, J. R. Ecker, J. Kaplan and M. L. Guerinot, *Science*, 2006, **314**, 1295.
10 M. D. de Jonge, C. Holzner, S. B. Baines, B. S. Twining, K. Ignatyev, J. Diaz, D. L. Howard, D. Legnini, A. Miceli, I. McNulty, C. J. Jacobsen and S. Vogt, *Proc. Natl. Acad. Sci. U. S. A.*, 2010, **107**, 15676.
11 G. McColl, S. A. James, S. Mayo, D. L. Howard, C. G. Ryan, R. Kirkham, G. F. Moorhead, D. Paterson, M. D. de Jonge and A. I. Bush, *PLoS One*, 2012, **7**, e32685.
12 B. L. Armbruster, E. Carlemalm, R. Chiovetti, R. M. Garavito, J. A. Hobot, E. Kellenberger and W. Villiger, *J. Microsc.*, 1982, **126**, 77.
13 B. Hornberger, M. D. De Jonge, M. Feser, P. Holl, C. Holzner, C. Jacobsen, D. Legnini, D. Paterson, P. Rehak and L. Struder, *J. Synchrotron Radiat.*, 2008, **15**, 355.
14 R. A. Barrea, D. Gore, N. Kujala, C. Karanfil, S. Kozyrenko, R. Heurich, M. Vukonich, R. Huang, T. Paunesku, G. Woloschak and T. C. Irving, *J. Synchrotron Radiat.*, 2010, **17**, 522.
15 S. Vogt, *J. Phys. IV*, 2003, **104**, 635.
16 *MATLAB*, Mathworks, Natick, MA, 2012.
17 G. L. Zeng, *Medical Image Reconstruction*, Higher Education Press, Beijing, and Springer, Heidelberg, 2010.
18 *Paraview 4.0*, Kitware, Inc., Clifton Park, New York, 2013.
19 C. A. Schneider, W. S. Rasband and K. W. Eliceiri, *Nat. Methods*, 2012, **9**, 671.
20 L. A. Shepp and Y. Vardi, *IEEE Trans. Med. Imaging*, 1982, **1**, 113.
21 E. X. Miqueles and A. R. De Pierro, *Comput. Phys. Commun.*, 2011, **182**, 2661.
22 E. Ho, S. Dukovcic, B. Hobson, C. P. Wong, G. Miller, K. Hardin, M. G. Traber and R. L. Tanguay, *Comp. Biochem. Physiol., Part C: Toxicol. Pharmacol.*, 2012, **155**, 26.
23 R. Bryson-Richardson, S. Berger and P. Currie, *Atlas of Zebrafish Development*, Elsevier Science, 2011.
24 C. B. Kimmel, W. W. Ballard, S. R. Kimmel, B. Ullmann and T. F. Schilling, *Dev. Dyn.*, 1995, **203**, 253.
25 L. H. Parker, L. I. Zon and D. Y. R. Stainier, *Methods Cell Biol.*, 1999, **59**, 313.
26 S. J. Nixon, R. I. Webb, M. Floetenmeyer, N. Schieber, H. P. Lo and R. G. Parton, *Traffic*, 2009, **10**, 131.
27 P. J. La Rivière, D. M. Billmire, P. A. Vargas, M. Rivers and S. Sutton, *Opt. Eng.*, 2006, **45**, 077005; E. X. Miqueles and A. R. De Pierro, *IEEE Trans. Med. Imaging*, 2011, **30**, 438; G. Fu, L.-J. Meng, P. Eng, M. Newville, P. Vargas and P. La Riviere, *Med. Phys.*, 2013, **40**, 061903.
28 R. S. MacDonald, *J. Nutr.*, 2000, **130**, 1500S.
29 L. Carvalho and C.-P. Heisenberg, *Trends Cell Biol.*, 2010, **20**, 586.
30 A. Donovan, A. Brownlie, Y. Zhou, J. Shepard, S. J. Pratt, J. Moynihan, B. H. Paw, A. Drejer, B. Barut, A. Zapata, T. C. Law, C. Brugnara, S. E. Lux, G. S. Pinkus, J. L. Pinkus, P. D. Kingsley, J. Palis, M. D. Fleming, N. C. Andrews and L. I. Zon, *Nature*, 2000, **403**, 776; S. P. Mudumana, H. Wan, M. Singh, V. Korzh and Z. Gong, *Dev. Dyn.*, 2004, **230**, 165.
31 N. E. Hellman and J. D. Gitlin, *Annu. Rev. Nutr.*, 2002, **22**, 439.
32 S. Korzh, A. Emelyanov and V. Korzh, *Mech. Dev.*, 2001, **103**, 137.
33 H. Ishizaki, M. Spitzer, J. Wildenhain, C. Anastasaki, Z. Q. Zeng, S. Dolma, M. Shaw, E. Madsen, J. Gitlin, R. Marais, M. Tyers and E. E. Patton, *Dis. Models & Mech.*, 2010, **3**, 639; S. R. G. Setty, D. Tenza, E. V. Sviderskaya, D. C. Bennett, G. Raposo and M. S. Marks, *Nature*, 2008, **454**, 1142.
34 B. L. Martin and D. Kimelman, *Curr. Biol.*, 2009, **19**, R215.
35 M. Sugiyama, A. Sakaue-Sawano, T. Iimura, K. Fukami, T. Kitaguchi, K. Kawakami, H. Okamoto, S. I. Higashijima and A. Miyawaki, *Proc. Natl. Acad. Sci. U. S. A.*, 2009, **106**, 20812.
36 J. P. Kanki and R. K. Ho, *Development*, 1997, **124**, 881.
37 R. McRae, B. Lai and C. J. Fahrni, *Metallomics*, 2013, **5**, 52.